



## Article

# Structural and Optical Properties of Graphene Quantum Dots–Polyvinyl Alcohol Composite Thin Film and Its Potential in Plasmonic Sensing of Carbaryl

Nurul Illya Muhamad Fauzi <sup>1</sup>, Yap Wing Fen <sup>1,2,\*</sup> , Faten Bashar Kamal Eddin <sup>2</sup> and Wan Mohd Ebtisyam Mustaqim Mohd Daniyal <sup>1</sup>

<sup>1</sup> Functional Nanotechnology Devices Laboratory, Institute of Nanoscience and Nanotechnology, Universiti Putra Malaysia, 43400 UPM Serdang, Selangor, Malaysia

<sup>2</sup> Department of Physics, Faculty of Science, Universiti Putra Malaysia, 43400 UPM Serdang, Selangor, Malaysia

\* Correspondence: yapwingfen@upm.edu.my

**Abstract:** In this study, graphene quantum dots (GQDs) and polyvinyl alcohol (PVA) composite was prepared and then coated on the surface of gold thin film via the spin coating technique. Subsequently, Fourier transform infrared spectroscopy (FT-IR), atomic force microscopy (AFM), and ultraviolet-visible spectroscopy (UV-Vis) were adopted to understand the structure, surface morphology, and optical properties of the prepared samples. The FT-IR spectral analysis revealed important bands, such as O–H stretching, C=O stretching, C–H stretching, and O=C=O stretching vibrations. The surface roughness of the GQDs-PVA composite thin film was found to be increased after exposure to carbaryl. On the other hand, the optical absorbance of the GQDs-PVA thin film was obtained and further analysis was conducted, revealing a band gap  $E_g$  value of 4.090 eV. The sensing potential of the thin film was analyzed using surface plasmon resonance (SPR) spectroscopy. The findings demonstrated that the developed sensor's lowest detection limit for carbaryl was 0.001 ppb, which was lower than that previously reported, i.e., 0.007 ppb. Moreover, other sensing performance parameters, such as full width at half maximum, detection accuracy, and signal-to-noise ratio, were also investigated to evaluate the sensor's efficiency.

**Keywords:** graphene quantum dots; polyvinyl alcohol; carbaryl; surface plasmon resonance



**Citation:** Fauzi, N.I.M.; Fen, Y.W.; Eddin, F.B.K.; Daniyal, W.M.E.M.M. Structural and Optical Properties of Graphene Quantum Dots–Polyvinyl Alcohol Composite Thin Film and Its Potential in Plasmonic Sensing of Carbaryl. *Nanomaterials* **2022**, *12*, 4105. <https://doi.org/10.3390/nano12224105>

Academic Editor: Iván Mora-Seró

Received: 21 October 2022

Accepted: 18 November 2022

Published: 21 November 2022

**Publisher's Note:** MDPI stays neutral with regard to jurisdictional claims in published maps and institutional affiliations.



**Copyright:** © 2022 by the authors. Licensee MDPI, Basel, Switzerland. This article is an open access article distributed under the terms and conditions of the Creative Commons Attribution (CC BY) license (<https://creativecommons.org/licenses/by/4.0/>).

## 1. Introduction

The last decade has witnessed an unprecedented number of studies investigating the synthesis and application of graphene-based materials, owing to their remarkable optical and mechanical properties [1–3]. Among the many members of the graphene family, graphene quantum dots (GQDs) are one of the most recent superstars of the carbon family. They have attracted significant attention because of their tunable band gap, which is caused by their smaller size than standard graphene sheets, excellent dispersibility, and biocompatibility [4–6]. Interestingly, GQDs can be compounded with solid materials and dispersed in common solvents [7,8]. To date, GQDs have demonstrated substantial potential in numerous applications, such as sensors [9], catalysis [10], energy devices [11,12], photothermal therapy [13,14], drug delivery [15], bioimaging [16,17], and solar cells [18]. Regarding optical sensing applications in the detection of pesticides, research indicates that synthesizing GQDs with a polymer can obtain highly sensitive material.

Based on literature analysis, several studies have detected pesticides using GQDs/magnetic silica beads-polyppyrrrole (PPy) [19], nitrogen-doped GQDs-polydopamine (PDA) [20], and sulfur-doped GQDs-polyvinyl alcohol (PVA) [21]. Among these materials, the PVA polymer has sparked considerable past and current interest, and studies are still being conducted to this day. PVA can also reportedly detect pesticides by synthesizing it with copper [22], encapsulated 5-aminofluorescein [23], cellulose silver nanoparticles [24], and gold nanoparticles [25,26]. It is

worth mentioning that all of the reported materials have been used to detect different types of pesticides. PVA has been widely used amidst a range of conducting and non-conducting polymers, owing to its availability in different molecular weights and affordability [27]. Furthermore, PVA is non-toxic and exhibits notable film-forming features, strong water solubility, easy processability, and is biocompatible and biodegradable [28–30]. These remarkable properties make PVA an ideal candidate for many applications, including gas sensors [31], biomedical devices [32], drug delivery [33], fuel cells, and membrane technology [34].

According to previous research exploring GQDs and PVA-based materials for the optical detection of pesticides, the most commonly used optical methods include fluorescence, photoluminescence, colorimetry, and surface-enhanced Raman spectroscopy [35–41]. Although the results obtained have been satisfactory, these methods have some limitations, including the need for sophisticated equipment, complicated procedures for pre-analysis, and they are time consuming. The surface plasmon resonance (SPR) method is expected to eliminate these problems. SPR corresponds to the free electrons on the surface of a metallic nanoparticle after being excited by the photons of incident light with a certain angle of incidence, which are then propagated parallel to the metal surface [42–49]. SPR is also a highly effective approach for the optical and label-free detection of tiny molecules, possessing advantages, including simple and low-cost fabrication, noticeable sensitivity, and quick analysis times [50–57]. This approach is necessary to identify pesticides such as carbaryl (1-naphthyl N-methylcarbamate), which comprises one of the main agricultural pesticides used in the modern agricultural sector. This substance is dangerous for humans because it severely inhibits acetylcholine esterase and forms strong mutagenic N-nitrosocarbamates, which lead to nervous system problems [58,59]. Due to its toxicity and broad use, the detection of this environmental contaminant necessitates the development of sensitive analytical techniques to track levels of carbaryl and monitor bioaccumulation.

As the structural and optical properties of GQDs-PVA have not been extensively reported, this study attempted to characterize the structure, surface morphology, and optical properties of a GQDs-PVA nanocomposite using Fourier transform infrared spectroscopy (FT-IR), atomic force microscopy (AFM), and ultraviolet-visible spectroscopy (UV-Vis). Importantly, the fabrication of GQDs-PVA for carbaryl pesticide detection has yet to be investigated using SPR. Thus, this investigation will explore the potential sensing properties of GQDs-PVA for carbaryl. This study highlights that the future of GQDs research is boundless, particularly if upcoming studies focus on the ease of eco-friendly synthesis and improving GQDs-PVA materials.

## 2. Materials and Method

### 2.1. Material Preparation

PVA with an average molecular weight of 146,000–186,000 (87–89% hydrolyzed) and a stock solution (100 mg/mL) of carbaryl (98.0%) were obtained from Sigma-Aldrich (St. Louis, MO, USA). GQDs synthesized using the hydrothermal method (1 mg/mL) were provided by ACS Material (Pasadena, CA, USA). The solution emitted blue light (460 nm) when excited with a 365 nm UV beam. The purity of GQDs was more than 80% with a particle size of less than 5 nm. For preparation of the PVA solution, 2.0 g of PVA powder was mixed with 36 mL of deionized water. Then, the solution was stirred for 1 h with a magnetic stirrer at 90 °C. To generate the GQDs-PVA solution, the previously prepared PVA solution was mixed with the GQDs solution in a 1:1 volume ratio and stirred at room temperature for 30 min. Figure 1 shows the schematic preparation of the composite solution. Then, various concentrations of carbaryl solutions were prepared by diluting the appropriate amount in deionized water, using the diluting formula  $M_1V_1 = M_2V_2$ .

$M_1$  = Stock concentration

$V_1$  = Stock volume

$M_2$  = Desired concentration

$V_2$  = Desired volume

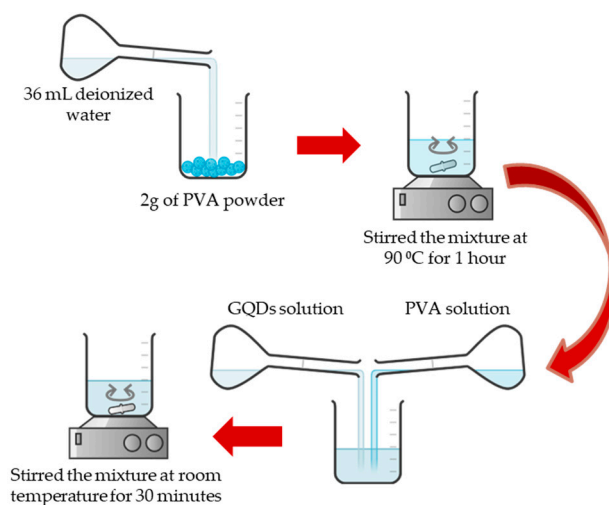


**Figure 1.** The schematic preparation of the composite solution.

### 2.2. Sensing Layer Preparation

First, the glass coverslip ( $24 \times 24 \times 0.1 \text{ mm}^3$ ) was cleaned with acetone to eliminate any fingerprint marks or grime on the glass surface. The glass slip was coated with a 50 nm gold thin film using the SC7640 Sputter (Quorum Technologies, West Sussex, UK). The gold-coated glass slip was then deposited with a QDs-PVA composite thin film using the spin coating method with the P-6708D Spin Coater (Inc. Medical Devices, Indianapolis, IN, USA). Approximately 0.50 mL of the sample solution was placed on the gold film and spun at 3000 rpm for 30 s. Figure 2 provides an overview of the steps involved in the thin film preparation process.

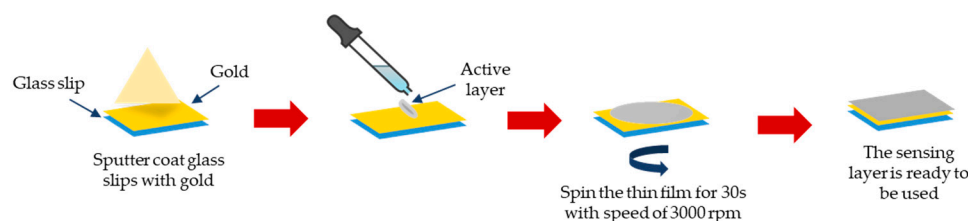


**Figure 2.** Steps involved in thin film preparation process.

### 2.3. Characterization

The FTIR spectra of the QDs, PVA, and QDs-PVA solutions were recorded using an ALPHA II FTIR Spectrometer (Bruker, CA, USA) in ATR mode. Then, the surface morphology of the QDs, PVA, and QDs-PVA thin films were examined by using the Dimension Edge AFM (Bruker, CA, USA) in intermittent mode, since this mode allows high resolution for fragile and thin samples. A UV-3600 UV-VIS-NIR spectrophotometer (Shimadzu, Japan) was used to measure the absorbance and band gap of all of the thin films.

### 2.4. SPR Spectroscopy

SPR occurs when a photon of incident light strikes a metal surface, usually a gold surface at specific conditions [60–62]. A component of the light energy couples with the metal surface layer's electrons through the metal coating at a specific angle of incidence, causing the electrons to move as a response to excitation [63,64]. In an SPR sensor setup, incident light is utilized using a glass prism with a high reflecting index in the Kretschmann configuration of the attenuated total reflection (ATR) method [65]. The refractive index of the material closer to the metal surface determines the stated SPR angle at which resonance occurs, under the conditions of a constant light source wavelength and thin metal surface [66]. Thus, detection is accomplished by observing the change in the reflected

light that is obtained on a detector. In this study, gold was used as the metal film because gold is inert, has high chemical stability, and efficiently absorbs light [67–70]. Then, GQDs-PVA was employed as an active layer to improve the sensitivity of the gold film for detecting pesticides. As a preliminary test, deionized water was injected into the cell, and the incidence angle for the reflectance curve was recorded as a reference. Subsequently, different carbaryl concentrations of 0.001, 0.008, 0.01, and 0.08 ppb were injected and left for 5 min to ensure that the carbaryl fully interacted with the GQDs-PVA layer. Figure 3 depicts the SPR spectroscopy sensor setup. The apparatus consisted of a laser, chopper, polarizer, sensor chip (gold layer and active layer), prism, photodiode, lock amplifier, stepper motor with resolution of  $0.001^\circ$ , and computer to display the changes in the reflected light.

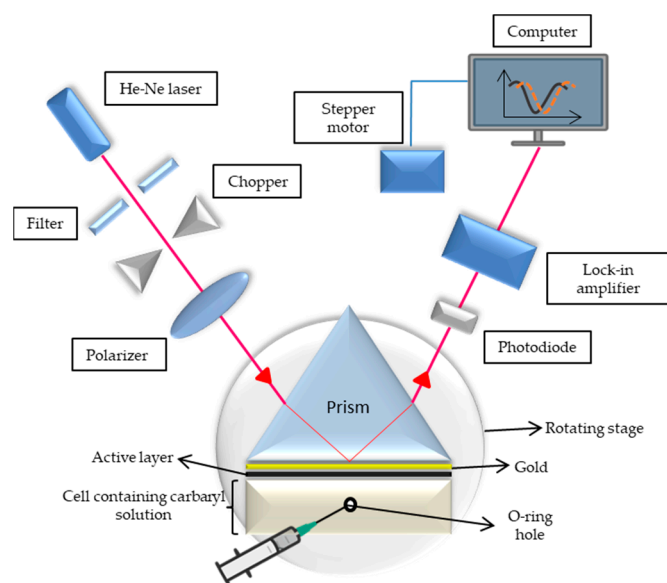


**Figure 3.** Schematic of surface plasmon resonance setup.

### 3. Results and Discussion

#### 3.1. Fourier Transform Infrared Spectroscopy

In this investigation, FTIR spectroscopy was used to identify the structural properties of GQDs, PVA, and GQDs-PVA films. For wavenumbers ranging from  $4000$  to  $600\text{ cm}^{-1}$ , the expected functional groups were revealed, consequently confirming the structures of all samples, as depicted in Figure 4. Referring to the FTIR spectrum of GQDs, the peak between  $3314$  and  $3694\text{ cm}^{-1}$  was due to the characteristic O-H stretching vibration. The bands at  $3075$ ,  $2867$ ,  $2145$ ,  $1767$ , and  $1150$ – $1616\text{ cm}^{-1}$  were assigned to C-H stretching (alkene), C-H stretching (alkane), which can indicate polycyclic aromatic hydrocarbons [71], C-N stretching, C=O stretching, and C-O stretching, respectively. Meanwhile, PVA exhibited the O-H stretching vibration, C-H stretching, O=C=O stretching, C-H bending of aromatic compounds, C=O stretching, C=C stretching, and C-O stretching, attributed to bands at  $3196$ – $3745$ ,  $2757$ ,  $2124$ ,  $1891$ – $1987$ ,  $1726$ ,  $1575$ , and  $1190\text{ cm}^{-1}$ , respectively. These results were consistent with those reported by Yang et al. in 2018 [72]. After immobilization of GQDs with PVA composite, O-H stretching became intense at wavenumbers  $3140$ – $3786\text{ cm}^{-1}$ . These results indicated that the reaction between GQDs functional groups and PVA groups occurred via interactions between the oxygenated groups in GQDs and the hydroxyl groups in PVA [73]. As can be seen in the FTIR spectrum of the GQDs-PVA film, C-H stretching (alkane), C-H stretching (alkene), O=C=O stretching, C=O stretching, C-O stretching, and C-H bending were attributed to bands at  $2866$ ,  $3059$ ,  $2180$ ,  $1780$ ,  $1616$ , and  $1465\text{ cm}^{-1}$ , respectively. The integration of GQDs with PVA resulted in the formation of common characteristics and also a new peak, which appeared to be due to C-H bending.

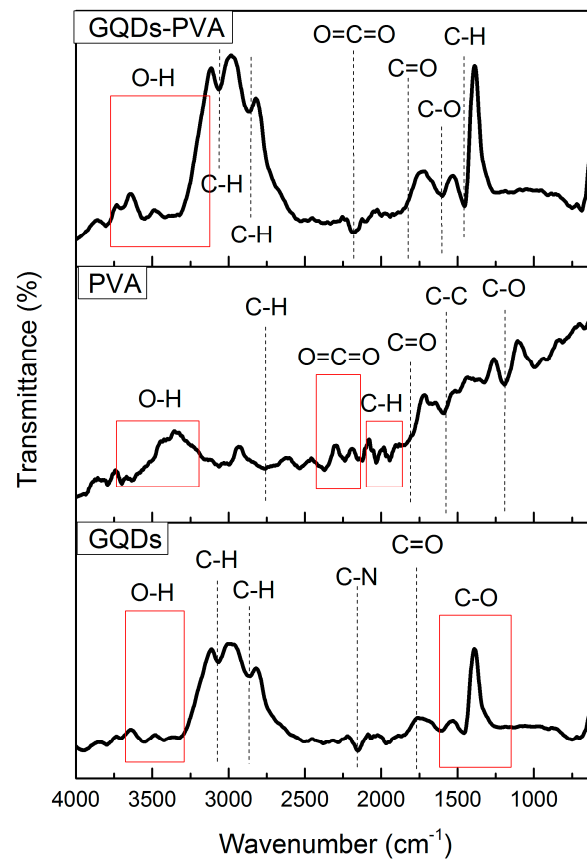


**Figure 4.** FTIR spectra of GQDs, PVA, and GQDs-PVA.

### 3.2. Surface Morphology

The roughness features of all spin-coated thin films were identified by AFM with the scan size fixed to  $2\ \mu\text{m} \times 2\ \mu\text{m}$ . Figures 5–8 show the AFM results for GQDs, PVA, GQDs-PVA, and GQDs-PVA after contact with carbaryl, following the composite materials being thoroughly coated on the surface of the gold thin film. As can be observed in Figure 5, the 2D image of the GQDs thin film revealed a relatively rough surface with a root mean square (RMS) roughness of 0.99 nm, similar to that observed by Anas et al. in 2019 [74]. Meanwhile, the 2D image of the PVA thin film in Figure 6 showed an even and circular surface structure, with an RMS roughness value of 2.86 nm. Then, the GQDs-PVA thin film in Figure 7 displayed an RMS roughness value of 1.12 nm with the surface appearance showing an even and granular structure. These changes in RMS roughness values may have been influenced by the formation of a network of GQDs nanoparticles with the PVA polymer [75]. After the GQDs-PVA thin film was exposed to carbaryl, the RMS roughness value increased to 1.38 nm, which proved the interaction of carbaryl with the GQDs-PVA thin film. The 2D image of the GQDs-PVA film after contact with carbaryl showed a fairly uniform surface structure with some white spots, which could be due to the carbaryl molecules, as depicted in Figure 8.

### 3.3. Optical Properties

The optical properties of the composite materials were observed based on the UV-Vis spectrum with a spectral resolution of 0.1 nm. Thus, the absorption spectra of GQDs, PVA, and GQDs-PVA thin films were obtained at different wavelengths, ranging from 200 to 500 nm. As can be observed in Figure 9, the absorbance of GQDs showed the highest value of 3.8 at 281.7 nm. Meanwhile, the absorbance of PVA showed the lowest value of 3.3 at 275.4 nm. After GQDs were immobilized with the PVA layer, the absorbance value was

approximately 3.7 at a wavelength of 276.3 nm. This peak may be attributed to the  $n-\pi^*$  transition of the carbonyl group, as presented in the FTIR analysis [76].

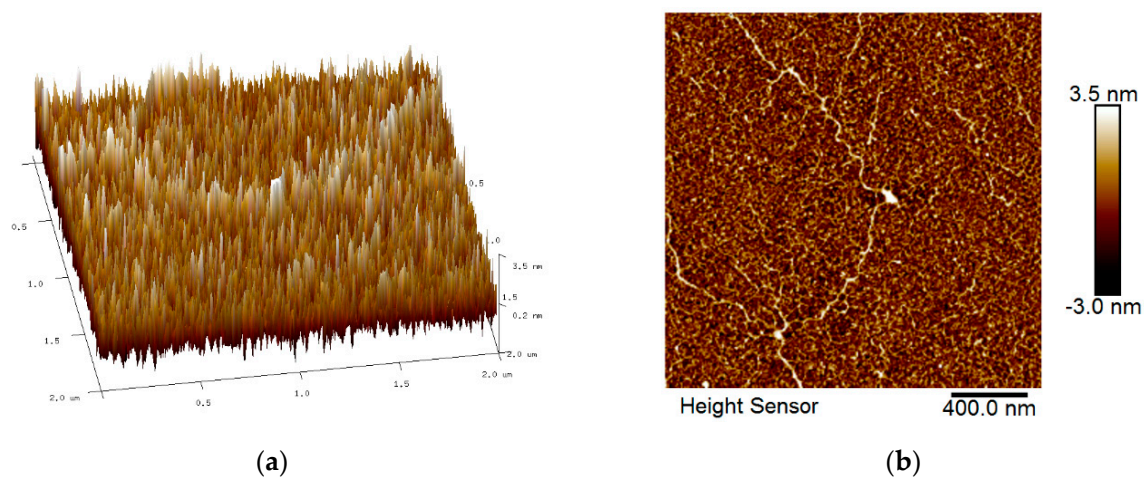


**Figure 5.** AFM images of GQDs thin film: (a) 3D image and (b) 2D image.

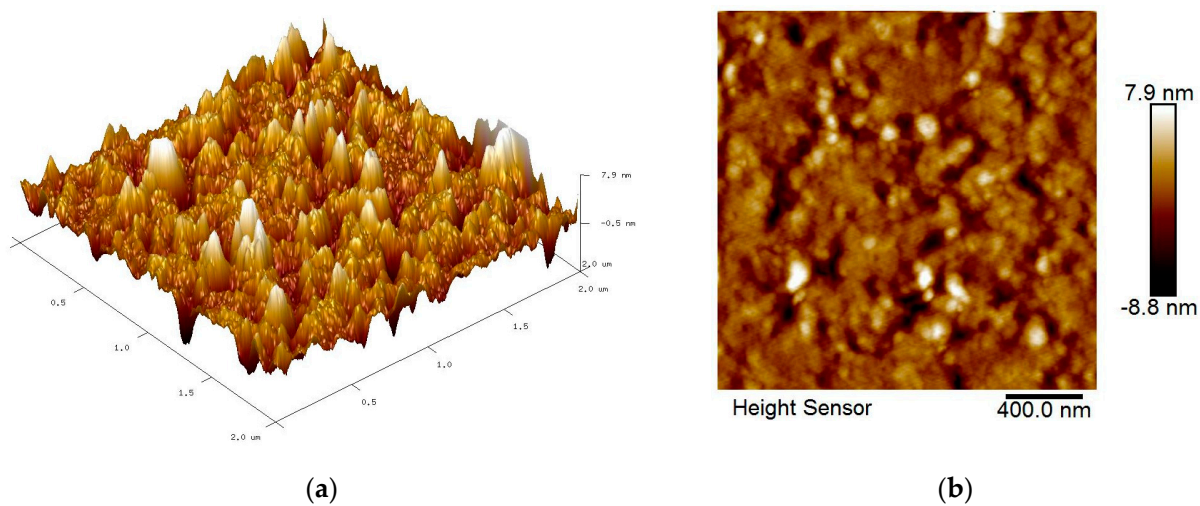


**Figure 6.** AFM images of PVA thin film: (a) 3D image and (b) 2D image.

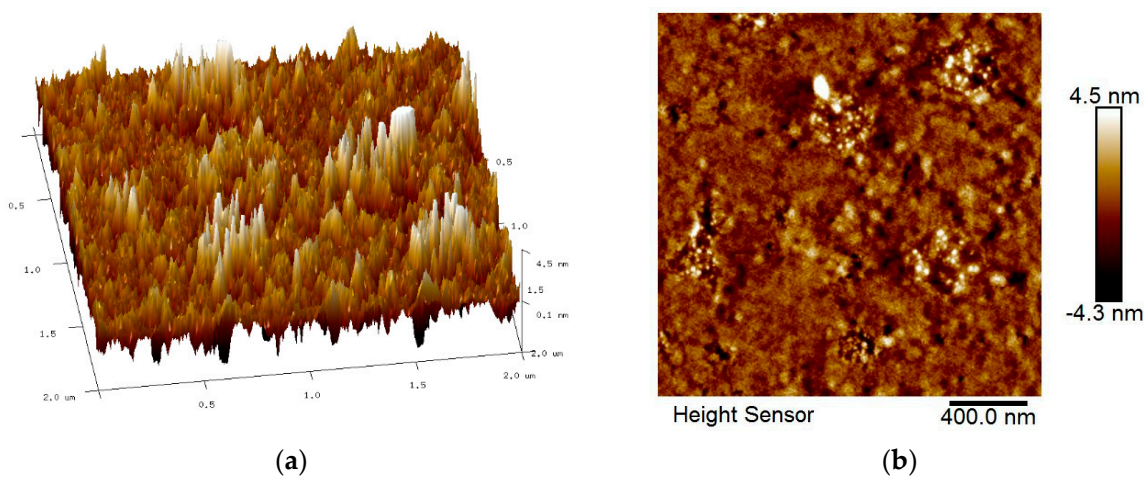


**Figure 7.** AFM images of GQDs-PVA thin film: (a) 3D image and (b) 2D image.

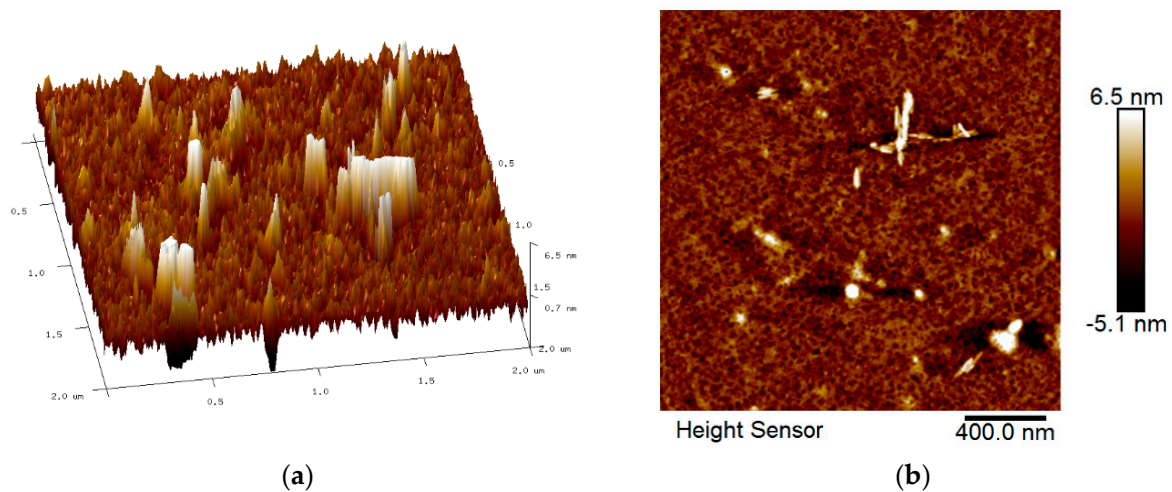


Figure 8. AFM images of GQDs-PVA thin film after contact with carbaryl: (a) 3D image and (b) 2D image.

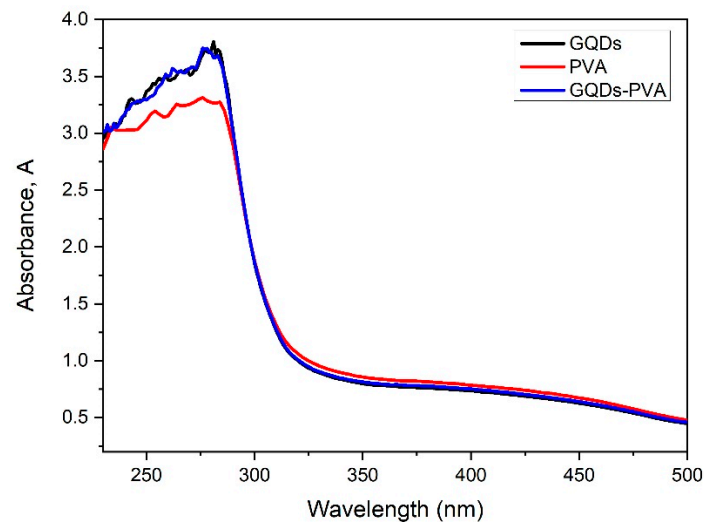


Figure 9. UV-Vis absorption spectra of GQDs, PVA, and GQDs-PVA thin films.

The absorbance,  $A$ , is one of the important parameters for obtaining the optical band gap value for samples. Therefore, Beer Lambert’s law was used to interpret the data, as shown in the equation below [77]:

$$a = 2.303 \frac{A}{t} \tag{1}$$

where  $a$  is the absorbance coefficient stated in units of  $\text{m}^{-1}$ , and  $t$  represents the sample thickness in meters (m). Then, the Tauc equation was followed [78]:

$$a = \frac{k(h\nu - E_g)^{\frac{1}{2}}}{h\nu} \tag{2}$$

where  $k$  indicates the constant value,  $h$  is Plank’s constant,  $h\nu$  represents the photon energy, and  $E_g$  indicates the band gap. Then, Equation (2) was derived to obtain Equation (3) below:

$$(ah\nu)^2 = k(h\nu - E_g) \tag{3}$$

Plotting the graph of  $(ah\nu)^2$  against  $h\nu$  was estimated to obtain the band gap for the GQDs, PVA, and GQDs-PVA thin films, respectively. By extracting the extrapolated straight lines on the  $x$ -axis from the Tauc equation, the optical band gaps were obtained for all samples [79].

Based on the graphs shown in Figures 10–12, the optical band gap of QDs was 4.087 eV, which aligned with the study by Bhatnagar et al. in 2017 [80]. The band gap for PVA was 4.061 eV and after QDs were immobilized, the energy band gap was increased to 4.100 eV. The possible reason that the energy band gap of QDs –PVA had the highest value compared to QDs and PVA alone might be due to the quantum confinement effect. In the quantum confinement phenomenon, electrons and nanoscale holes in the semiconductor are trapped or confined [81]. As a result, the energy difference between full and empty states increases or widens the semiconductor's band gap. According to Zhu et al. in 2017, the band gap in a quantum dot crystal is size dependent and can be altered to provide a range of energies between the valence and conduction bands. Additionally, because of quantum confinement, the band gap energy of a quantum dot increases as its size decreases [82].

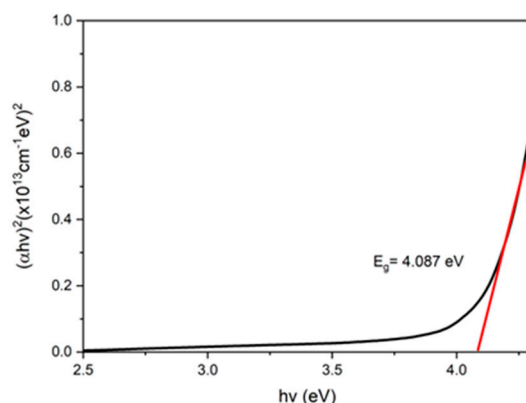


Figure 10. UV-Vis band gap energy of QDs thin film.

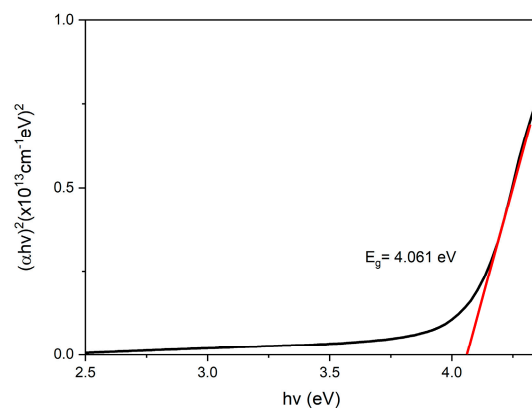


Figure 11. UV-Vis band gap energy of PVA thin film.

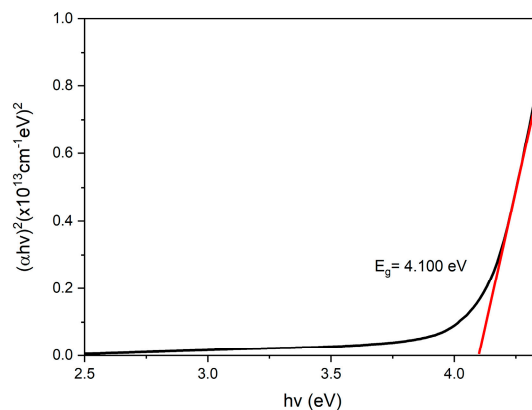
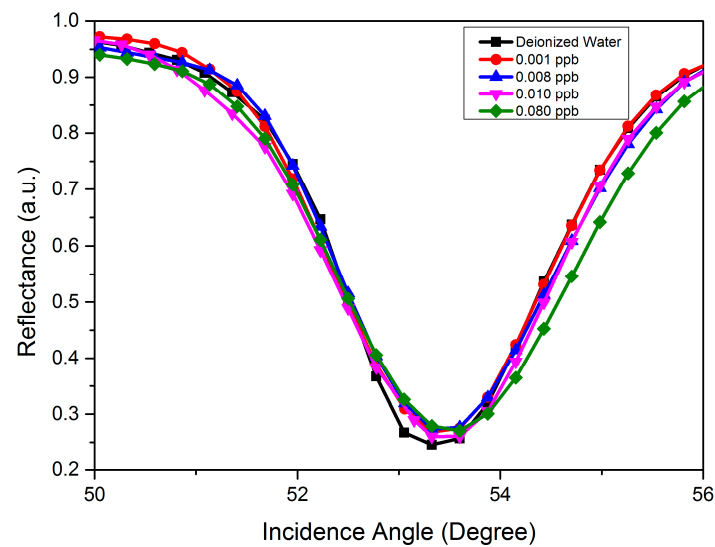


Figure 12. UV-Vis band gap energy of QDs-PVA thin film.

### 3.4. Potential Plasmonic Sensing

In the initial SPR analysis, the gold thin film was used as a baseline to compare the gold-modified GQDs-PVA layer. As a preliminary test, deionized water was injected into the cell and the incidence angle for the reflectance curve was recorded as a reference. Then, injections of carbaryl concentrations at 0.001, 0.008, 0.01, and 0.08 ppb were recorded. During the analysis, a sharp dip in the curve was obtained at a specific incidence angle that corresponded to the resonance angle, which resulted from the reflected light reduced because of the efficient transfer of energy to surface plasmons. As shown in Figure 13, the incidence angle for the reflectance curve of the gold thin film was recorded at  $53.323^\circ$ . As expected, the gold thin film had a weak binding capacity and was unable to distinguish changes in the refractive index of different concentrations of carbaryl, which led to approximately the same shift of the resonance angle.



**Figure 13.** SPR reflectance curve as a function of incidence angle for gold thin film in the detection of different concentrations of carbaryl.

Then, the SPR analysis was continued by modifying the gold thin film with the GQDs-PVA solution. The SPR spectra for the GQDs-PVA sensor films in contact with deionized water and all concentrations of carbaryl are shown in Figure 14. The resonance angle obtained for deionized water was  $53.694^\circ$  while the resonance angle for carbaryl concentrations of 0.001, 0.008, 0.01, and 0.08 ppb were  $53.709^\circ$ ,  $53.787^\circ$ ,  $53.809^\circ$ , and  $54.390^\circ$ , respectively. The resonance angles increased and shifted slightly to the right with increasing carbaryl concentrations. The resonance angle incremental increasing trend can be attributed to the absorbed carbaryl filling the space between the GQDs-PVA layers. This finding was supported by previous research reporting that GQDs-PVA has a reticular structure to which small molecules can attach [75]. Moreover, electron changes on the surface of the GQDs-PVA also occurred in the presence of carbaryl adsorption, which led to changes in the refractive index when the carbaryl concentration increased. The electrons involved were probably from the  $\text{COOH}^-$  anion in GQDs and  $\text{NH}_3^+$  cation in carbaryl. It also must be pointed out that this investigation had a limit of detection of 0.001 ppb, which was a lower limit detection than that reported by previous studies detecting carbaryl using various optical methods [36–41,83–90]. Comparisons with other studies are listed in Table 1.

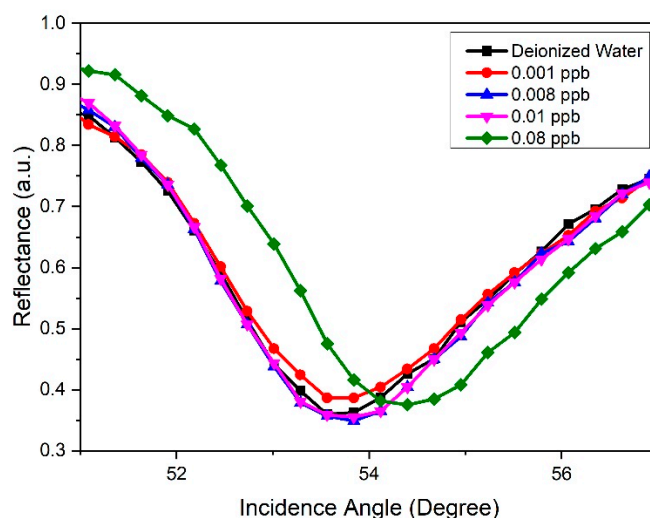


**Figure 14.** SPR reflectance curve as a function of incidence angle for GQDs-PVA thin film in the detection of different concentrations of carbaryl.

**Table 1.** Comparison of this study with other carbaryl sensors using various materials in terms of limit of detection.

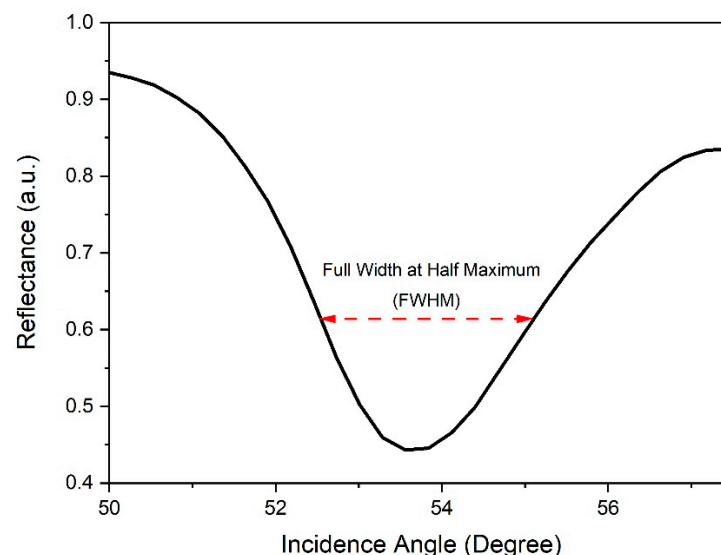
Method	Material	Limit of Detection (ppb)	Reference
Surface plasmon resonance	Monoclonal antibody	1.380	[36]
	Gold modified GQDs-PVA	0.001	This study
Colorimetry	Idophenyl acetate-acetylcholinesterase	2.010	[37]
	Gold nanoparticles	1.500	[38]
	Silver reduced-graphene oxide Carbon quantum dots-AuNPs-acetylcholinesterase	0.200	[39]
	p-acetamidobenzenesulfonyl azide-AuNPs	50.000	[83]
Fluorescence	Cadmium telluride quantum dots	0.120	[40]
	Graphene quantum dots	0.360	[88]
	3,5-di(2',5'-dicarboxylphenyl)pyridine	6.700	[89]
	Flavourzyme-stabilized gold nanoclusters	0.470	[90]
Photoluminescence	Silicon quantum dots- acetylcholinesterase/choline oxidase	0.007	[84]
Chemiluminescence	Lum-AgNP	1000	[85]
Colorimetry and Chemiluminescence	Dual-graphitic carbon nitride/bismuth ferrite	0.033	[86]
High Fundamental Frequency Quartz Crystal Microbalance	Monoclonal antibody	0.050	[87]
Liquid Chromatography with tandem mass spectrometry	Acetylcholinesterase	20.000	[41]

To analyze the sensing parameters of GQDs-PVA thin film in the detection of carbaryl, the shift of resonance angle was introduced [91]. Based on the data in Table 2, the shift of the resonance angle was calculated by subtracting the resonance angle of different carbaryl concentrations from the resonance angle of deionized water. As a result, the shift of the resonance angle increased with increasing carbaryl concentration when in contact with GQDs-PVA thin film [92].

**Table 2.** The resonance angle and shift of resonance angle for the detection of various concentrations of carbaryl (0–0.08 ppb).

Concentration of Carbaryl (ppb)	Resonance Angle, $\theta$ (Degree)	Shift of Resonance Angle, $\Delta\theta$ (Degree)
0	53.694	0
0.001	53.709	0.015
0.008	53.787	0.093
0.01	53.809	0.115
0.08	54.390	0.697

Full width at half maximum (FWHM) is a parameter that can indicate a sensor's efficiency and accuracy [93]. The FWHM can be evaluated as the distance between the curve points at half the maximum peak level of the reflectance curve, as shown in Figure 15. Theoretically, a lower FWHM value indicates a sharper reflectance curve, which represents better sensor accuracy [94]. Through the FWHM data, detection accuracy (DA) can be obtained. DA is defined as the ratio of the shift of the resonance angle relative to the FWHM [95]. Therefore, DA is inversely proportional to the FWHM. In this analysis, the FWHM was experimentally measured from the reflectance curve for GQDs-PVA thin film after interaction with different concentrations of carbaryl.

**Figure 15.** Illustration of FWHM, which represents half of the maximum value on the reflectance curve (for deionized water).

As shown in Figure 16, the FWHM was increased from  $3.043^\circ$  to  $3.090^\circ$  when the carbaryl concentration increased from 0.001 to 0.01 ppb. Then, from 0.01 to 0.08 ppb, the FWHM value decreased to  $2.930^\circ$ . Based on the data obtained, the trend in FWHM outcomes was not particularly stable. It fluctuates between increases and declines. As mentioned before, the FWHM value has an inverse relationship with DA, where a lower FWHM value gives better sensor detection accuracy. Thus, in this analysis, the detection of 0.08 ppb carbaryl was attributed to the smaller FWHM value of  $2.930^\circ$  and highest DA value of  $0.341 \text{ degree}^{-1}$ .

Another important performance parameter of an SPR sensor is the signal-to-noise ratio (SNR). In other words, the SNR is evaluated to compare the level of the desired signal to the background noise [96]. In this SPR analysis, the value of the resonance angle shift was multiplied by DA to identify the SNR, as shown in Equation (4) below:

$$SNR = \frac{\Delta\theta_{SPR}}{FWHM} = \Delta\theta_{SPR} \times DA \quad (4)$$

From the data obtained for SNR values using Equation (4), the evolution of SNR with increasing carbaryl concentration was plotted. As illustrated in Figure 17, increasing the carbaryl concentration appeared to reduce the noise in the SPR signal, resulting in higher SNR values for the suggested sensor.

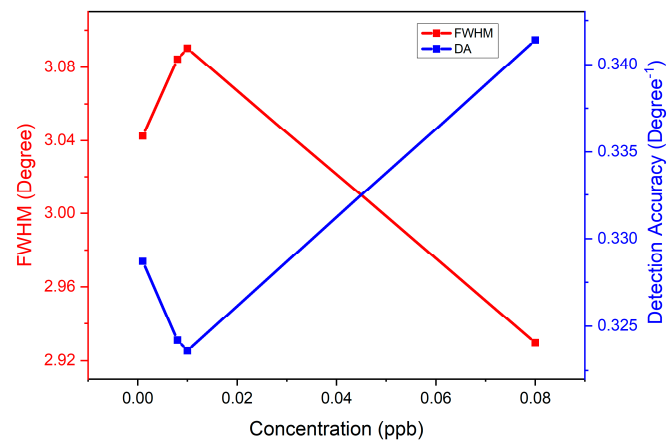


Figure 16. Graph of FWHM and DA versus concentration of carbaryl.

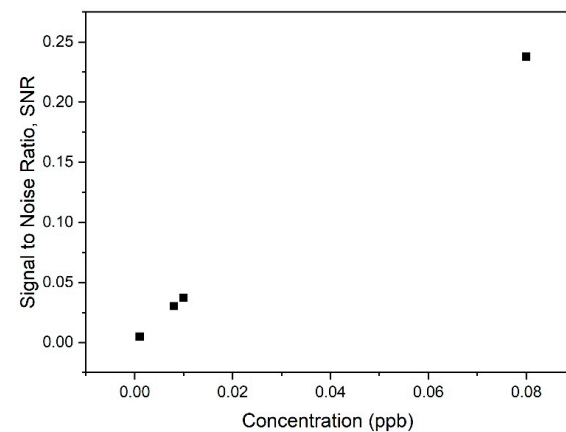


Figure 17. Graph of SNR versus carbaryl concentration.

Table 3 summarizes the FWHM, DA, and SNR values for GQDs-PVA thin film in the detection of various concentrations of carbaryl. Based on the results presented, the best FWHM was obtained at the higher concentration of carbaryl (0.08 ppb) with a value of 2.930°. Notably, FWHM values are inversely proportional to DA values. Thus, in this analysis, 0.08 ppb carbaryl was detected at the highest DA value of 0.341 degree<sup>-1</sup>.

Table 3. The FWHM, DA, and SNR values for GQDs-PVA thin film in the detection of carbaryl (0.001–0.08 ppb).

Concentration of Carbaryl (ppb)	Full Width Half Maximum (Degree)	Detection Accuracy (Degree <sup>-1</sup> )	Signal-to-Noise-Ratio
0.001	3.043	0.329	0.005
0.008	3.084	0.324	0.030
0.01	3.090	0.324	0.037
0.08	2.930	0.341	0.238

#### 4. Conclusions

In this work, GQDs-PVA was successfully prepared using a simple chemical method and coated on gold film using the spin coating technique. Then, the structure, surface morphology, and optical and sensing properties were analyzed. FTIR analysis determined that the structure of the GQDs synthesized with PVA had the main components of O-H bonding, C=O bonding, C-H bonding, and O=C=O bonding. AFM analysis revealed that the surface morphology of the GQDs was affected by PVA with the appearance of a granular structure for GQDs-PVA. In addition, the value of RMS roughness increased after GQDs-PVA thin film was exposed to carbaryl solution and the surface became fairly uniform with white spots. Subsequently, the UV-Vis spectra of the thin films were evaluated to obtain the direct band gap of GQDs-PVA. This composite material had the highest energy band gap, 4.100 eV, compared to the single elements. Thus, the optical band gap data revealed that the GQDs-PVA exhibited semiconducting behavior. The GQDs-PVA thin film was investigated by SPR for potential sensing of carbaryl, where it showed high potential with a limit of detection of 0.001 ppb. Therefore, this study reveals the huge potential of GQDs-PVA for optical sensor applications in the detection of pesticides.

**Author Contributions:** Conceptualization, N.I.M.F.; methodology, N.I.M.F.; software, W.M.E.M.M.D.; validation, Y.W.F.; formal analysis, F.B.K.E.; investigation, N.I.M.F.; writing—original draft preparation, N.I.M.F.; writing—review and editing, Y.W.F., F.B.K.E. and W.M.E.M.M.D.; visualization, N.I.M.F.; supervision, Y.W.F.; funding acquisition, Y.W.F. All authors have read and agreed to the published version of the manuscript.

**Funding:** This research was funded by the Ministry of Education of Malaysia through the FRGS (FRGS/1/2019/STG02/UPM/02/1) and Universiti Putra Malaysia through the Putra Grant (GP-IPB/2021/9700700).

**Data Availability Statement:** Not applicable.

**Acknowledgments:** The authors are grateful to the Institute of Nanoscience and Nanotechnology, Department of Physics and Department of Chemistry, Faculty of Science, Universiti Putra Malaysia for providing all the facilities.

**Conflicts of Interest:** The authors declare no conflict of interest.

#### References

1. Riesen, H.; Wiebeler, C.; Schumacher, S. Optical spectroscopy of graphene quantum dots: The case of C132. *J. Phys. Chem.* **2014**, *118*, 5189–5195.
2. Kalluri, A.; Debnath, D.; Dharmadhikari, B.; Patra, P. Chapter Twelve—Graphene quantum dots: Synthesis and applications. *Methods Enzymol.* **2018**, *609*, 335–354. [[PubMed](#)]
3. Rahmandoust, M. Computational evaluation of the mechanical properties of synthesized graphene quantum dots under consideration of defects. *Carbon Lett.* **2020**, *31*, 427–440. [[CrossRef](#)]
4. Zheng, X.T.; Ananthanarayanan, A.; Luo, K.Q.; Chen, P. Glowing graphene quantum dots and carbon dots: Properties, syntheses, and biological applications. *Nano Micro Small* **2015**, *11*, 1620–1636. [[CrossRef](#)] [[PubMed](#)]
5. Lee, N.E.; Jeong, J.; Lim, H.S.; Lee, S.Y.; Cho, S.O. Ultraviolet/blue light emitting high-quality graphene quantum dots and their biocompatibility. *Carbon N. Y.* **2020**, *170*, 213–219. [[CrossRef](#)]
6. Zhu, C.; Yang, S.; Wang, G.; Mo, R.; He, P.; Sun, J.; Di, Z.; Yuan, N.; Ding, J.; Ding, G.; et al. Negative induction effect of “graphite” N on graphene quantum dots: Tunable band gap photoluminescence. *J. Mater. Chem. C* **2015**, *3*, 8810–8816. [[CrossRef](#)]
7. Chen, Z.; Wang, D.; Wang, X.; Yang, J. Preparation and formaldehyde sensitive properties of N-GQDs/SnO<sub>2</sub> nanocomposite. *Chin. Chem. Lett.* **2019**, *31*, 2063–2066. [[CrossRef](#)]
8. Khojasteh, H.; Salavati-niasari, M.; Safajou, H.; Safardoust-hojaghan, H. Facile reduction of graphene using urea in solid phase and surface modification by N-doped graphene quantum dots for adsorption of organic dyes. *Diam. Relat. Mater.* **2017**, *79*, 133–144.
9. Li, M.; Chen, T.; Gooding, J.J.; Liu, J. A review of carbon and graphene quantum dots for sensing. *ACS Sens.* **2019**, *4*, 1732–1748. [[CrossRef](#)]
10. Yan, Y.; Gong, J.; Chen, J.; Zeng, Z.; Huang, W.; Pu, K.; Liu, J.; Chen, P. Recent advances on graphene quantum dots: From chemistry and physics to applications. *Adv. Mater.* **2019**, *31*, 1808283. [[CrossRef](#)]
11. Prabhu, S.A.; Kavithayeni, V.; Suganthi, R.; Geetha, K. Graphene quantum dots synthesis and energy application: A review. *Carbon Lett.* **2021**, *31*, 1–12. [[CrossRef](#)]

12. Yang, S.; Li, W.; Ye, C.; Wang, G.; Tian, H.; Zhu, C.; He, P.; Ding, G.; Xie, X.; Liu, Y.; et al. C<sub>3</sub>N—A 2D crystalline, hole-free, tunable-narrow-bandgap semiconductor with ferromagnetic properties. *Adv. Mater.* **2017**, *29*, 1605625. [[CrossRef](#)] [[PubMed](#)]
13. Fan, H.; Yu, X.; Wang, K.; Yin, Y.; Tang, Y.; Tang, Y.; Liang, X. Graphene quantum dots (GQDs)-based nanomaterials for improving photodynamic therapy in cancer treatment. *Eur. J. Med. Chem.* **2019**, *182*, 111620. [[CrossRef](#)] [[PubMed](#)]
14. Li, J.; Yang, S.; Deng, Y.; Chai, P.; Yang, Y.; He, X.; Xie, X.; Kang, Z.; Ding, G.; Zhou, H.; et al. Emancipating target-functionalized carbon dots from autophagy vesicles for a novel visualized tumor therapy. *Adv. Funct. Mater.* **2018**, *28*, 1800881. [[CrossRef](#)]
15. Zhao, C.; Song, X.; Liu, Y.; Fu, Y.; Ye, L.; Wang, N.; Wang, F.; Li, L.; Mohammadniaei, M.; Zhang, M.; et al. Synthesis of graphene quantum dots and their applications in drug delivery. *J. Nanobiotechnol.* **2020**, *18*, 142. [[CrossRef](#)]
16. Chung, S.; Revia, R.A.; Zhang, M. Graphene quantum dots and their applications in bioimaging, biosensing, and therapy. *Adv. Mater.* **2021**, *33*, 1–26. [[CrossRef](#)]
17. Li, Y.; Dong, H.; Tao, Q.; Ye, C.; Yu, M.; Li, J.; Zhou, H.; Yang, S.; Ding, G.; Xie, X. Enhancing the magnetic relaxivity of MRI contrast agents via the localized superacid microenvironment of graphene quantum dots. *Biomaterials* **2020**, *250*, 120056. [[CrossRef](#)]
18. Mahalingam, S.; Manap, A.; Omar, A.; Low, F.W.; Afandi, N.F.; Chia, C.H.; Rahim, N.A. Functionalized graphene quantum dots for dye-sensitized solar cell: Key challenges, recent developments and future prospects. *Renew. Sustain. Energy Rev.* **2021**, *144*, 110999. [[CrossRef](#)]
19. Zor, E.; Morales-Narváez, E.; Zamora-Gálvez, A.; Bingol, H.; Ersoz, M.; Merkoçi, A. Graphene quantum dots-based photoluminescent sensor: A multifunctional composite for pesticide detection. *ACS Appl. Mater. Interfaces* **2015**, *36*, 20272–20279. [[CrossRef](#)]
20. Liu, Y.; Cao, N.; Gui, W.; Ma, Q. Nitrogen-doped graphene quantum dots-based fluorescence molecularly imprinted sensor for thiocloprid detection. *Talanta* **2018**, *183*, 339–344. [[CrossRef](#)]
21. Nair, R.V.; Thomas, R.T.; Mohamed, A.P.; Pillai, S. Fluorescent turn-off sensor based on sulphur-doped graphene quantum dots in colloidal and film forms for the ultrasensitive detection of carbamate pesticides. *Microchem. J.* **2020**, *157*, 104971. [[CrossRef](#)]
22. De Almeida, L.K.S.; Chigome, S.; Torto, N.; Frost, C.L.; Pletschke, B.I. A novel colorimetric sensor strip for the detection of glyphosate in water. *Sens. Actuators B Chem.* **2015**, *206*, 357–363. [[CrossRef](#)]
23. Aksornneam, L.; Kanatharana, P.; Thavarungkuai, P.; Thammakhet, C. 5-aminofluorescein doped polyvinyl alcohol film for the detection of formaldehyde in vegetables and seafood. *Anal. Methods* **2016**, *8*, 1249–1256. [[CrossRef](#)]
24. Thi, P.; Hong, K.; Jang, C. Sensitive and label-free liquid crystal-based optical sensor for the detection of malathion. *Anal. Biochem.* **2020**, *593*, 113589.
25. Chamuah, N.; Bhuyan, N.; Das, P.P.; Ojah, N.; Choudhary, A.J.; Medhi, T.; Nath, P. Gold-coated electrospun PVA nano fibers as SERS substrate for detection of pesticides. *Sens. Actuators B Chem.* **2018**, *273*, 710–717. [[CrossRef](#)]
26. Kong, L.; Huang, M.; Chen, J.; Lin, M. In situ detection of thiram in fruits and vegetables by colorimetry/surface-enhanced Raman spectroscopy. *Laser Phys.* **2020**, *30*, 65602. [[CrossRef](#)]
27. Solaro, R.; Corti, A.; Chiellini, E. Biodegradation of poly (vinyl alcohol) with different molecular weights and degree of hydrolysis. *Polym. Adv. Technol.* **2000**, *878*, 873–878. [[CrossRef](#)]
28. Zhang, Y.; Liu, X.; Wu, X.; Liu, Q.; Wang, Z. A carbon black/polyvinyl alcohol-based composite thin film sensor integrating strain and humidity sensing using the droplet deposition method. *Crystals* **2022**, *12*, 1316. [[CrossRef](#)]
29. Liu, B.; Zhang, J.; Guo, H. Research progress of polyvinyl alcohol water-resistant film materials. *Membranes* **2022**, *12*, 347. [[CrossRef](#)]
30. Kouser, S.; Prabhu, A.; Prashantha, K.; Nagaraja, G.K.; Neetha, J.; Navada, K.M.; Qurashi, A.; Manasa, D.J. Modified halloysite nanotubes with Chitosan incorporated PVA/PVP bionanocomposite films: Thermal, mechanical properties and biocompatibility for tissue engineering. *Colloids Surf. A Physicochem. Eng. Asp.* **2022**, *634*, 127941. [[CrossRef](#)]
31. El Fawal, G.F.; Hassan, S.; El-aassar, M.R.; Elkady, M.F. Electrospun polyvinyl alcohol nanofibers containing titanium dioxide for gas sensor applications. *Arab. J. Sci. Eng.* **2019**, *44*, 251–257. [[CrossRef](#)]
32. Husain, M.S.B.; Gupta, A.; Alashwal, B.Y.; Sharma, S. Synthesis of PVA/PVP based hydrogel for biomedical applications: A review. *Energy Sources Part A Recover. Util. Environ. Eff.* **2018**, *40*, 2388–2393. [[CrossRef](#)]
33. Shagholani, H.; Ghoreishi, S.M.; Mousazadeh, M. Improvement of interaction between PVA and chitosan via magnetite nanoparticles for drug delivery application. *Int. J. Biol. Macromol.* **2015**, *78*, 130–136. [[CrossRef](#)] [[PubMed](#)]
34. de Souza Gomes, A.; Filho, J.C.D. Hybrid membranes of PVA for direct ethanol fuel cells (DEFCs) applications. *Int. J. Hydrogen Energy* **2012**, *37*, 6246–6252. [[CrossRef](#)]
35. Fauzi, N.I.M.; Fen, Y.W.; Omar, N.A.S.; Hashim, H.S. Recent advances on detection of insecticides using optical sensors. *Sensors* **2021**, *21*, 3856. [[CrossRef](#)] [[PubMed](#)]
36. Mauriz, E.; Calle, A.; Abad, A.; Montoya, A.; Hildebrandt, A.; Barcel, D.; Lechuga, L.M. Determination of carbaryl in natural water samples by a surface plasmon resonance flow-through immunosensor. *Biosens. Bioelectron.* **2006**, *21*, 2129–2136. [[CrossRef](#)] [[PubMed](#)]
37. Hossain, S.M.Z.; Luckham, R.E.; McFadden, M.J.; Brennan, J.D. Reagentless bidirectional lateral flow bioactive paper sensors for detection of pesticides in beverage and food samples. *Anal. Chem.* **2009**, *81*, 9055–9064. [[CrossRef](#)]
38. Minha, P.N.; Hoangb, V.-T.; Ngo Xuan Dinh; Van Hoang, O.; Van Cuong, N.; Hop, D.T.B.; Tuanc, T.Q.; Khi, N.T.; Huy, T.Q.; Le, A.-T. Reduced graphene oxide-wrapped silver nanoparticles for applications to ultrasensitive colorimetric detection of Cr (VI) ions and carbaryl pesticide. *New J. Chem.* **2020**, *44*, 7611–7620. [[CrossRef](#)]

39. Chen, Y.; Qin, X.; Yuan, C.; Shi, R.; Wang, Y. Double responsive analysis of carbaryl pesticide based on carbon quantum dots and Au nanoparticles. *Dye. Pigment.* **2020**, *181*, 108529. [[CrossRef](#)]
40. Shahdost-fard, F.; Fahimi-Kashani, N.; Hormozi-nezhad, M. A ratiometric fluorescence nanoprobe using CdTe QDs for fast detection of carbaryl insecticide in apple. *Talanta* **2020**, *221*, 121467. [[CrossRef](#)]
41. Tsagkaris, A.S.; Uttl, L.; Pulkrabova, J.; Hajslova, J. Screening of carbamate and organophosphate pesticides in food matrices using an affordable and simple spectrophotometric acetylcholinesterase assay. *Appl. Sci.* **2020**, *10*, 565. [[CrossRef](#)]
42. Arcadio, F.; Seggio, M.; Prete, D.D.; Buonanno, G.; Mendes, J.; Coelho, L.C.C.; Jorge, P.A.S.; Zeni, L.; Bossi, A.M.; Cennamo, N. A plasmonic biosensor based on light-diffusing fibers functionalized with molecularly imprinted nanoparticles for ultralow sensing of proteins. *Nanomaterials* **2022**, *9*, 1400. [[CrossRef](#)] [[PubMed](#)]
43. Ramdzan, N.S.M.; Fen, Y.W.; Omar, N.A.S.; Anas, N.A.A.; Liew, J.Y.C.; Daniyal, W.M.E.M.M.; Hashim, H.S. Detection of mercury ion using surface plasmon resonance spectroscopy based on nanocrystalline cellulose/poly (3,4-ethylenedioxythiophene) thin film. *Measurement* **2021**, *182*, 109728. [[CrossRef](#)]
44. Daniyal, W.M.E.M.M.; Fen, Y.W.; Jaafar, A.; Sadrolhosseini, A.R.; Mahdi, M.A. Design and optimization of surface plasmon resonance spectroscopy for optical constant characterization and potential sensing application: Theoretical and experimental approaches. *Photonics* **2021**, *8*, 361. [[CrossRef](#)]
45. Hashim, H.S.; Fen, Y.W.; Omar, N.A.S.; Abdullah, J.; Daniyal, W.M.E.M.M.; Saleviter, S. Detection of phenol by incorporation of gold modified-enzyme based graphene oxide thin film with surface plasmon resonance technique. *Opt. Express* **2020**, *28*, 9738–9752. [[CrossRef](#)]
46. Fauzi, N.I.M.; Fen, Y.W.; Jaafar, A.; Kamarudin, M.A.; Omar, N.A.S.; Eddin, F.B.K.; Ramdzan, N.S.M.; Daniyal, M.E.M.M. Evaluation of structural and optical properties of graphene oxide-polyvinyl alcohol thin film and its potential for pesticide detection using an optical method. *Photonics* **2022**, *9*, 300. [[CrossRef](#)]
47. Eddin, F.B.K.; Fen, Y.W. The principle of nanomaterials based surface plasmon resonance biosensors and its potential for dopamine detection. *Molecules* **2020**, *25*, 2769. [[CrossRef](#)]
48. Park, J.H.; Cho, Y.W.; Kim, T.H. Recent advances in surface plasmon resonance sensors for sensitive optical detection of pathogens. *Biosensors* **2022**, *3*, 180. [[CrossRef](#)]
49. Potdar, R.P.; Kholam, Y.B.; Shaikh, S.F.; More, P.S.; Rana, A.H. Polyvinylpyrrolidone-capped silver nanoparticles for highly sensitive and selective optical fiber-based ammonium sensor. *Nanomaterials* **2022**, *19*, 3373. [[CrossRef](#)]
50. Singh, P. SPR biosensors: Historical perspectives and current challenges. *Sens. Actuators B Chem.* **2016**, *229*, 110–130. [[CrossRef](#)]
51. Eddin, F.B.K.; Fen, Y.W.; Fauzi, N.I.M.; Daniyal, W.M.E.M.M.; Omar, N.A.S.; Anuar, M.F.; Hashim, H.S.; Sadrolhosseini, A.R.; Abdullah, H. Direct and sensitive detection of dopamine using carbon quantum dots based refractive index surface plasmon resonance sensor. *Nanomaterials* **2022**, *12*, 1799. [[CrossRef](#)] [[PubMed](#)]
52. Puiu, M.; Bala, C. SPR and SPR Imaging: Recent trends in developing nanodevices for detection and real-time monitoring of biomolecular events. *Sensors* **2016**, *6*, 870. [[CrossRef](#)] [[PubMed](#)]
53. Saleviter, S.; Fen, Y.W.; Daniyal, W.M.E.M.M.; Abdullah, J.; Sadrolhosseini, A.R.; Omar, N.A.S. Design and analysis of surface plasmon resonance optical sensor for determining cobalt ion based on chitosan-graphene oxide decorated quantum dots-modified gold active layer. *Opt. Express* **2019**, *27*, 32294–32307. [[CrossRef](#)] [[PubMed](#)]
54. Ramdzan, N.S.M.; Fen, Y.W.; Anas, N.A.A.; Omar, N.A.S.; Saleviter, S. Development of biopolymer and conducting polymer-based optical sensors for heavy metal ion detection. *Molecules* **2020**, *25*, 2548. [[CrossRef](#)]
55. Fauzi, N.I.M.; Fen, Y.W.; Omar, N.A.S.; Saleviter, S.; Daniyal, W.M.E.M.M.; Hashim, H.S.; Nasrullah, M. Nanostructured chitosan/maghemite composites thin film for potential optical detection of mercury ion by surface plasmon resonance investigation. *Polymers* **2020**, *12*, 1497. [[CrossRef](#)]
56. Ashley, J.; Piekarska, M.; Segers, C.; Trinh, L.; Rodgers, T.; Willey, R.; Tothill, I.E. An SPR based sensor for allergens detection. *Biosens. Bioelectron.* **2017**, *88*, 109–113. [[CrossRef](#)]
57. Fen, Y.W.; Yunus, W.M.M.; Moksini, M.M.; Talib, Z.A.; Yusof, N.A. Surface plasmon resonance optical sensor for mercury ion detection by crosslinked chitosan thin film. *J. Optoelectron. Adv. Mater.* **2011**, *13*, 279–285.
58. Pope, C.; Karanth, S.; Liu, J. Pharmacology and toxicology of cholinesterase inhibitors: Uses and misuses of a common mechanism of action. *Environ. Toxicol. Pharmacol.* **2005**, *19*, 433–446. [[CrossRef](#)]
59. Leung, M.C.K.; Meyer, J.N. Mitochondria as a target of organophosphate and carbamate pesticides: Revisiting common mechanisms of action with new approach methodologies. *Reprod. Toxicol.* **2019**, *89*, 83–92. [[CrossRef](#)]
60. Rosddi, N.N.M.; Fen, Y.W.; Anas, N.A.A.; Omar, N.A.S.; Ramdzan, N.S.M.; Daniyal, W.M.E.M.M. Cationically modified nanocrystalline cellulose/carboxyl-functionalized graphene quantum dots nanocomposite thin film: Characterization and potential sensing application. *Crystals* **2020**, *10*, 875. [[CrossRef](#)]
61. Fen, Y.W.; Yunus, W.M.M.; Yusof, N.A. Optical properties of cross-linked chitosan thin film for copper ion detection using surface plasmon resonance technique. *Opt. Appl.* **2011**, *41*, 999–1013.
62. Omar, N.A.S.; Fen, Y.W.; Abd, J.; Yasmin, M. Sensitive detection of dengue virus type 2 E-Proteins signals using self-assembled monolayers/reduced graphene oxide-PAMAM dendrimer thin film-SPR optical sensor. *Sci. Rep.* **2020**, *10*, 2374. [[CrossRef](#)] [[PubMed](#)]

63. Roshidi, M.D.A.; Fen, Y.W.; Omar, N.A.S.; Saleviter, S.; Daniyal, W.M.E.M.M. Optical studies of graphene oxide/poly(amidoamine) dendrimer composite thin film and its potential for sensing Hg<sup>2+</sup> using surface plasmon resonance spectroscopy. *Sens. Mater.* **2019**, *31*, 1147–1156. [[CrossRef](#)]
64. Saleviter, S.; Fen, Y.W.; Omar, N.A.S.; Daniyal, W.M.E.M.M.; Abdullah, J.; Zaid, M.H.M. Structural and optical studies of cadmium sulfide quantum dot- graphene oxide-chitosan nanocomposite thin film as a novel SPR spectroscopy active layer. *J. Nanomater.* **2018**, *2018*, 1–8. [[CrossRef](#)]
65. Daniyal, W.M.E.M.M.; Fen, Y.W.; Anas, N.A.A.; Omar, N.A.S.; Ramdzan, N.S.M.; Nakajima, H.; Mahdi, M.A. Enhancing the sensitivity of a surface plasmon resonance-based optical sensor for zinc ion detection by the modification of a gold thin film. *RSC Adv.* **2019**, *9*, 41729–41736. [[CrossRef](#)] [[PubMed](#)]
66. Daniyal, W.M.E.M.M.; Fen, Y.W.; Fauzi, N.I.M.; Hashim, H.S.; Ramdzan, N.S.; Omar, N.A.S. Recent advances in surface plasmon resonance optical sensors for potential application in environmental monitoring. *Sens. Mater.* **2020**, *32*, 4191–4200. [[CrossRef](#)]
67. Li, Z.; Munro, K.; Ebralize, I.I.; Narouz, M.R.; Padmos, J.D.; Hao, H.; Crudden, C.M.; Horton, J.H. N-heterocyclic carbene self-assembled monolayers on gold as surface plasmon resonance biosensors. *J. Am. Chem. Soc.* **2017**, *49*, 13936–13944. [[CrossRef](#)]
68. Ramdzan, N.S.; Fen, Y.W.; Liew, J.Y.C.; Omar, N.A.S.; Anas, N.A.A.; Daniyal, W.M.E.M.M.; Fauzi, N.I.M. Exploration on structural and optical properties of nanocrystalline cellulose/poly(3,4-ethylenedioxythiophene) thin film for potential plasmonic sensing application. *Photonics* **2021**, *8*, 419. [[CrossRef](#)]
69. Hashim, H.S.; Fen, Y.W.; Omar, N.A.S.; Daniyal, W.M.E.M.M.; Saleviter, S.; Abdullah, J. Structural, optical and potential sensing properties of tyrosinase immobilized graphene oxide thin film on gold surface. *Optik—Int. J. Light Electron Opt.* **2020**, *212*, 164786. [[CrossRef](#)]
70. Jin, Y.; Kang, X.; Song, Y.; Zhang, B.; Cheng, G.; Dong, S. Controlled nucleation and growth of surface-confined gold nanoparticles on a (3-aminopropyl)trimethoxysilane-modified glass slide: A strategy for SPR substrates. *Anal. Chem.* **2001**, *73*, 2843–2849. [[CrossRef](#)]
71. Paterno, G.M.; Goudappagouda; Chen, Q.; Lanzani, G.; Scotognella, F.; Narita, A. Large polycyclic aromatic hydrocarbons as graphene quantum dots: From synthesis to spectroscopy and photonics. *Adv. Opt. Mater.* **2021**, *9*, 2100508. [[CrossRef](#)]
72. Yang, S.; Lei, P.; Shan, Y.; Zhang, D. Preparation and characterization of antibacterial electrospun chitosan/poly(vinyl) alcohol/graphene oxide composite nanofibrous membrane. *Appl. Surf. Sci.* **2018**, *435*, 832. [[CrossRef](#)]
73. Salunke, A.S.; Salunke, S.T.; Deokate, R.J.; Kale, B.B. Tuning of photoluminescence behavior of gold coated chitosan-polyvinyl alcohol binding with graphene quantum dots. *Mater. Today Proc.* **2022**, *62*, 1752–1757. [[CrossRef](#)]
74. Anas, N.A.A.; Fen, Y.W.; Omar, N.A.S.; Ramdzan, N.S.M.; Daniyal, W.M.E.M.M.; Saleviter, S.; Zainudin, A.A. Optical properties of chitosan/hydroxyl-functionalized graphene quantum dots thin film for potential optical detection of ferric (III) ion. *Opt. Laser Technol.* **2019**, *120*, 105724. [[CrossRef](#)]
75. Zhao, Y.; Tong, R.J.; Chen, M.Q.; Xia, F. Relative humidity sensor based on hollow core fiber filled with QGDs-PVA. *Sens. Actuators B Chem.* **2019**, *284*, 96–102. [[CrossRef](#)]
76. Felipe, B.H.S.; Cabral, R.L.B.; Ladchumananandasivam, R.; Zille, A.; Kim, S.; Fehine, P.B.A.; Nascimento, J.H.O. Nanocoating on cotton fabric with nitrogen-doped graphene quantum dots/titanium dioxide/PVA: An erythematous UV protection and photoluminescent finishin. *J. Mater. Res. Technol. J.* **2022**, *18*, 2435–2450. [[CrossRef](#)]
77. Swinehart, D.F. The Beer-Lambert Law. *J. Chem. Educ.* **1962**, *39*, 333–335. [[CrossRef](#)]
78. Sangiorgi, N.; Aversa, L.; Tatti, R.; Verucchi, R.; Sanson, A. Spectrophotometric method for optical band gap and electronic transitions determination of semiconductor materials. *Opt. Mater.* **2017**, *64*, 18–25. [[CrossRef](#)]
79. Abdulla, H.S.; Abbo, A.I. Optical and electrical properties of thin films of polyaniline and polypyrrole. *Int. J. Electrochem. Sci.* **2012**, *7*, 10666–10678.
80. Bhatnagar, D.; Singh, S.; Yadav, S.; Kumar, A.; Kaur, I. Experimental and theoretical investigation of relative optical band gaps in graphene generations. *Mater. Res. Express* **2017**, *4*, 15101. [[CrossRef](#)]
81. Efros, A.L.; Nesbitt, D.J. Origin and control of blinking in quantum dots. *Nat. Publ. Gr.* **2016**, *11*, 661–671. [[CrossRef](#)] [[PubMed](#)]
82. Zhu, S.; Song, Y.; Wang, J.; Wan, H.; Zhang, Y.; Ning, Y. Photoluminescence mechanism in graphene quantum dots: Quantum confinement effect and surface/edge state. *Nano Today* **2017**, *13*, 10–14. [[CrossRef](#)]
83. Qi, Y.Y.; Tai, Z.X.; Sun, D.F.; Chen, J.T.; Ma, H.B.; Yan, X.B.; Liu, B.; Xue, Q.J. Fabrication and characterization of poly (vinyl alcohol)/graphene oxide nanofibrous biocomposite scaffolds. *J. Appl. Polym. Sci.* **2012**, *127*, 1885–1894. [[CrossRef](#)]
84. Yi, Y.; Zhu, G.; Liu, C.; Huang, Y.; Zhang, Y.; Li, H.; Zhao, J.; Yao, S. A Label-free silicon quantum dots-based photoluminescence sensor for ultrasensitive detection of pesticides. *Anal. Chem.* **2013**, *85*, 11464–11470. [[CrossRef](#)] [[PubMed](#)]
85. He, Y.; Xu, B.; Li, W.; Yu, H. Silver nanoparticle-based chemiluminescent sensor array for pesticide discrimination. *J. Agric. Food Chem.* **2015**, *63*, 2930–2934. [[CrossRef](#)] [[PubMed](#)]
86. Zhang, C.; Cui, H.; Cai, J.; Duan, Y.; Liu, Y. Development of fluorescence sensing material based on CdSe/ZnS quantum dots and molecularly imprinted polymer for the detection of carbaryl in rice and chinese cabbage. *J. Agric. Food Chem.* **2015**, *63*, 5–11. [[CrossRef](#)]
87. Cervera-chiner, L.; Carmen, M.; Antonio, A. Detection of DDT and carbaryl pesticides in honey by means of immunosensors based on High Fundamental Frequency Quartz Crystal Microbalance (HFF-QCM). *J. Sci. Food Agric.* **2020**, *100*, 2468–2472. [[CrossRef](#)]

88. Soriano, M.L.; Jimenez-Sanchez, A.; Cardenas, S. Passivated graphene quantum dots for carbaryl determination in juices. *J. Sep. Sci.* **2021**, *44*, 1652–1661. [[CrossRef](#)]
89. Zhang, Y.; Gao, L.; Ma, S.; Hu, T. Porous MB@Cd-MOF obtained by post-modification: Self-calibrated fluorescent turn-on sensor for highly sensitive detection of carbaryl. *Cryst. Growth Des.* **2022**, *22*, 2662–2669. [[CrossRef](#)]
90. Chen, J.; Liu, Z.; Fang, J.; Wang, Y.; Cao, Y.; Xu, W.; Ma, Y.; Meng, X.; Wang, B. A turn-on fluorescence biosensor for sensitive detection of carbaryl using flavourzyme-stabilized gold nanoclusters. *LWT* **2022**, *157*, 113099. [[CrossRef](#)]
91. Fen, Y.W.; Mahmood, W.; Yunus, M.; Yusof, N.A. Detection of mercury and copper ions using surface plasmon resonance optical sensor. *Sens. Materials* **2011**, *23*, 325–334.
92. Omar, N.A.S.; Fen, Y.W.; Abdullah, J.; Zaid, M.H.M.; Daniyal, W.M.E.M.M.; Mahdi, M.A. Sensitive surface plasmon resonance performance of cadmium sulfide quantum dots-amine functionalized graphene oxide based thin film towards dengue virus E-protein. *Opt. Laser Technol.* **2019**, *114*, 204–208. [[CrossRef](#)]
93. Maharana, P.K.; Srivastava, T. On the performance of highly sensitive and accurate graphene-on-aluminum and silicon-based SPR biosensor for visible and near infrared. *Plasmonics* **2014**, *9*, 1113–1120. [[CrossRef](#)]
94. Chiu, N.; Tu, Y.; Huang, T. Enhanced sensitivity of anti-symmetrically structured surface plasmon resonance sensors with zinc oxide intermediate layers. *Sensors* **2014**, *14*, 170–187. [[CrossRef](#)] [[PubMed](#)]
95. Rahman, M.S.; Rikta, K.A.; Faisal, L.; Anower, M.S. Enhanced performance of SnSe-Graphene hybrid photonic surface plasmon refractive sensor for biosensing applications. *Photonics Nanostruct.-Fundam. Appl.* **2020**, *39*, 100779. [[CrossRef](#)]
96. Sharma, A.K.; Gupta, B.D. On the sensitivity and signal to noise ratio of a step-index fiber optic surface plasmon resonance sensor with bimetallic layers. *Opt. Commun.* **2005**, *245*, 159–169. [[CrossRef](#)]